

Towards Accurate and Interpretable Neuroblastoma Diagnosis via Contrastive Multi-scale Pathological Image Analysis

Zhu Zhu, Shuo Jiang, Jingyuan Zheng, Yawen Li, Yifei Chen,
Manli Zhao, Weizhong Gu, Feiwei Qin, Jinhu Wang and Gang Yu

Abstract—Neuroblastoma, adrenal-derived, is among the most common pediatric solid malignancies, characterized by significant clinical heterogeneity. Timely and accurate pathological diagnosis from hematoxylin and eosin-stained whole-slide images is critical for patient prognosis. However, current diagnostic practices primarily rely on subjective manual examination by pathologists, leading to inconsistent accuracy. Existing automated whole-slide image classification methods encounter challenges such as poor interpretability, limited feature extraction capabilities, and high computational costs, restricting their practical clinical deployment. To overcome these limitations, we propose CMSwinKAN, a contrastive-learning-based multi-scale feature fusion model tailored for pathological image classification, which enhances the Swin Transformer architecture by integrating a Kernel Activation Network within its multilayer perceptron and classification head modules, significantly improving both interpretability and accuracy. By fusing multi-scale features and leveraging contrastive learning strategies, CMSwinKAN mimics clinicians’ comprehensive approach, effectively capturing global and local tissue characteristics. Additionally, we introduce a heuristic soft voting mechanism guided by clinical insights to seamlessly bridge patch-level predictions to whole-slide image-level classifications. We validate CMSwinKAN on the PpNTs dataset, which was collaboratively established with our partner hospital and the publicly accessible BreakHis dataset. Results demonstrate that CMSwinKAN performs better than existing state-of-the-art pathology-specific models pre-trained on large datasets. Our source code is available at <https://github.com/JSliam94/CMSwinKAN>.

Index Terms—Neuroblastoma, Pathological Image, Classification, Kernel Activation Network, Multi-Scale Fusion

I. INTRODUCTION

This work was supported by the National Key Research and Development Program of China under Grant 2023YFC2706400, and the Medical Health Science and Technology Project of Zhejiang Provincial Health Commission under Grant 2023KY832. (Zhu Zhu, Shuo Jiang, and Jingyuan Zheng contributed equally to this work.) (Corresponding authors: Gang Yu; Jinhu Wang; Feiwei Qin.)

Zhu Zhu, Yawen Li, Manli Zhao, Weizhong Gu, Jinhu Wang and Gang Yu are with Children’s Hospital, Zhejiang University School of Medicine, Hangzhou, 310000, China (e-mail: {zhuzhu.cs; yawen.li; zhaomanli; 6195013; wjh; yugbme}@zju.edu.cn).

Shuo Jiang, Jingyuan Zheng and Feiwei Qin are with the Hangzhou Dianzi University, Hangzhou 310018, China (e-mail: {jiangshuo; zhengjoy; qinfeiwei}@hdu.edu.cn).

Yifei Chen is with the Tsinghua University, Beijing 100084, China (e-mail: justlfc03@gmail.com).

PERIPHERAL neuroblastic tumors (pNTs) are malignant tumors originating in the developing sympathetic nervous system and represent the most common solid extracranial tumors in children [1], accounting for 15% of all childhood cancer-related deaths [2]. Due to the multiple subtypes of pNTs, significant differences exist in each subtype’s pathological characteristics and corresponding treatment strategies. Thus, precise subtype classification is critical for risk stratification and the development of personalized treatment plans. At present, pathological diagnosis is the gold standard for diagnosing pNTs. However, due to the subtle pathological differences between subtypes, diagnosis in clinical practice primarily relies on manual examination by pathologists, which is characterized by significant subjectivity and limitations [3, 4]. It is challenging to perform a holistic evaluation of whole-slide images (WSIs). Therefore, developing automated methods to precisely identify cytopathological morphologies across entire WSIs and achieve accurate subtype diagnosis has become an urgent need.

Previous studies have developed automated whole slide imaging (WSI) diagnostic methods [5, 6], but several challenges remain. First, current feature representation capabilities are inadequate, with conventional machine learning relying on handcrafted features that fall short in capturing pathological details and tissue variations. While deep learning has improved upon feature extraction [7], conventional convolutional neural networks (CNNs) still struggle with the complexity of histopathology images, limiting their ability to capture long-range dependencies and multi-scale features [8]. This issue can reduce the robustness of these models in clinical settings [9]. Furthermore, the lack of model interpretability complicates clinical deployment, as deep learning models often act as “black boxes,” leading to increased risks and diminished pathologist confidence in their outputs [10]. These interpretability challenges significantly limit the use of automated diagnostic tools in practice [11].

The size of WSI can reach giga pixels, which often exceeds a graphics processing unit (GPU) memory capacity [12]. Consequently, the common practice is to divide these images into multiple patches for classification. However, this patch-level processing leads to challenges like information fragmentation and false associations [13]. It may overlook essential spatial structures and disrupt critical lesion regions,

resulting in reduced diagnostic accuracy. Thus, a classification model with strong interpretability is urgently needed that better integrates local details with global context, offers strong feature representation for clinical applications.

To tackle these issues, this study proposes CMSwinKAN, a contrastive multi-scale feature fusion model for patch-level classification in pNTs subtyping, with a tissue-aware soft voting mechanism for WSI-level analysis on hematoxylin and eosin (H&E)-stained pathological images. Our main contributions are as follows:

- **Multi-scale interaction and contrastive learning:** We propose a contrast-driven multi-scale feature fusion framework (CMSA) that incorporates contrastive learning and fusion across multi-scale features. This framework adaptively adjusts the contributions of features at different scales, capturing both long-range dependencies and local details in histopathological images. It resolves the insufficient interaction between multi-scale features by mitigating the negative impact of low information density in feature representation.
- **Lightweight and interpretable deep architecture:** We introduce a multi-head self-attention module with a combined configuration of regular and shifted windows (Swin KANsformer Block) and integrate a Kernel Activation Network (KAN) as the classification head. This significantly enhances the model’s feature representation and nonlinear modeling performance.
- **Soft voting mechanism for WSI-level classification:** We propose a WSI classification method using clinical prior knowledge and a soft voting mechanism. By training a support vector machine (SVM), we achieve fine-grained tissue component recognition at the patch level. This approach integrates local and global features through a dynamic weight allocation strategy, enhancing classification accuracy and robustness.

II. RELATED WORKS

A. Traditional Computer Vision Models in Pathology

Traditional methods for pathological image classification rely on handcrafted features, which struggle with high-resolution images. Gheisari et al. [14] used Scale-Invariant Feature Transform and SVM to classify NB pathological images into five subtypes but only achieved 68.2% accuracy due to limited feature expressiveness. An improvement with a Convolutional Deep Belief Network (CDBN) extracted higher-level patterns and reached an F1 score of 86.01% using the Shimada classification system [15]. However, this approach faced challenges like low computational efficiency and difficulty modeling long-range spatial dependencies due to the high resolution of WSIs.

To address the high-resolution nature of WSIs, patch-based CNN methods have become mainstream. Hou et al. [16] proposed a decision fusion model that improved recognition performance by integrating local patch classification results. However, its “independent processing-simple fusion” approach led to fragmented spatial information. Recently, Li et al. [17] proposed a weakly supervised method based on the Variational

Information Bottleneck, further refining the optimization of feature representation. While this method performed well on multiple datasets, its patch-level processing still fell short in capturing global structural information effectively.

B. Development of Pathology Large Models

Recent advances in self-supervised learning (SSL) have propelled breakthroughs in large pathology models. For instance, Wang et al. [18] proposed the CTransPath model, which combines CNNs with a multi-scale Swin Transformer architecture, achieving state-of-the-art (SOTA) performance across multiple pathology tasks. Additionally, Chen et al. introduced the universal pathology pretraining model UNI, which was pre-trained on over 1 million pathological images. UNI surpassed existing methods across 34 pathology tasks, achieving comprehensive breakthroughs from tissue classification to cancer subtype prediction [19].

The introduction of vision-language models has further enhanced the generalization capabilities of large pathology models. Lu et al. [20] proposed the CONCH model, which was pre-trained on 1.17 million image-text pairs in a task-agnostic manner, achieving leading performance in tasks such as pathological image classification, segmentation, and retrieval. Furthermore, Azizi et al. [21] developed the REMEDIS framework, which improved the robustness of medical image models through SSL.

C. Advantages of Lightweight Small Models

Pathology large models exhibit four main limitations: high computational resource demands (e.g., months of GPU pre-training), limited deployability on medical edge devices, lack of interpretability, and poor adaptability to small-sample datasets like pediatric tumors.

In contrast, lightweight, small models offer unique advantages in terms of computational efficiency and adaptability. For example, Zormpas-Petridis et al. [22] proposed the Super-Histopath framework, which uses the Simple Linear Iterative Clustering superpixel algorithm to segment low-resolution WSIs and classify superpixels based on CNNs, enabling precise mapping of tumor heterogeneity. Ding et al. [23] introduced the Fuzzy-Guided Multi-Granularity Deep Neural Network (FMDNN), which effectively simulates pathologists’ multi-level diagnostic processes and performs well on public datasets.

In the field of efficient Transformer design, Stegmüller et al. [24] proposed ScoreNet, which uses a differentiable recommendation mechanism to focus on the most discriminative pathological regions and incorporates the ScoreMix data augmentation strategy to enhance generalization. Additionally, Liu et al. [25] developed the DetexNet network, which combines Texture Energy Measure to improve the representation ability of low-level pathological features, enabling high accuracy on small-sample pathology datasets. These methods are more efficient than large models but still struggle to capture local features like nuclear details and tissue patterns while integrating multi-scale information.

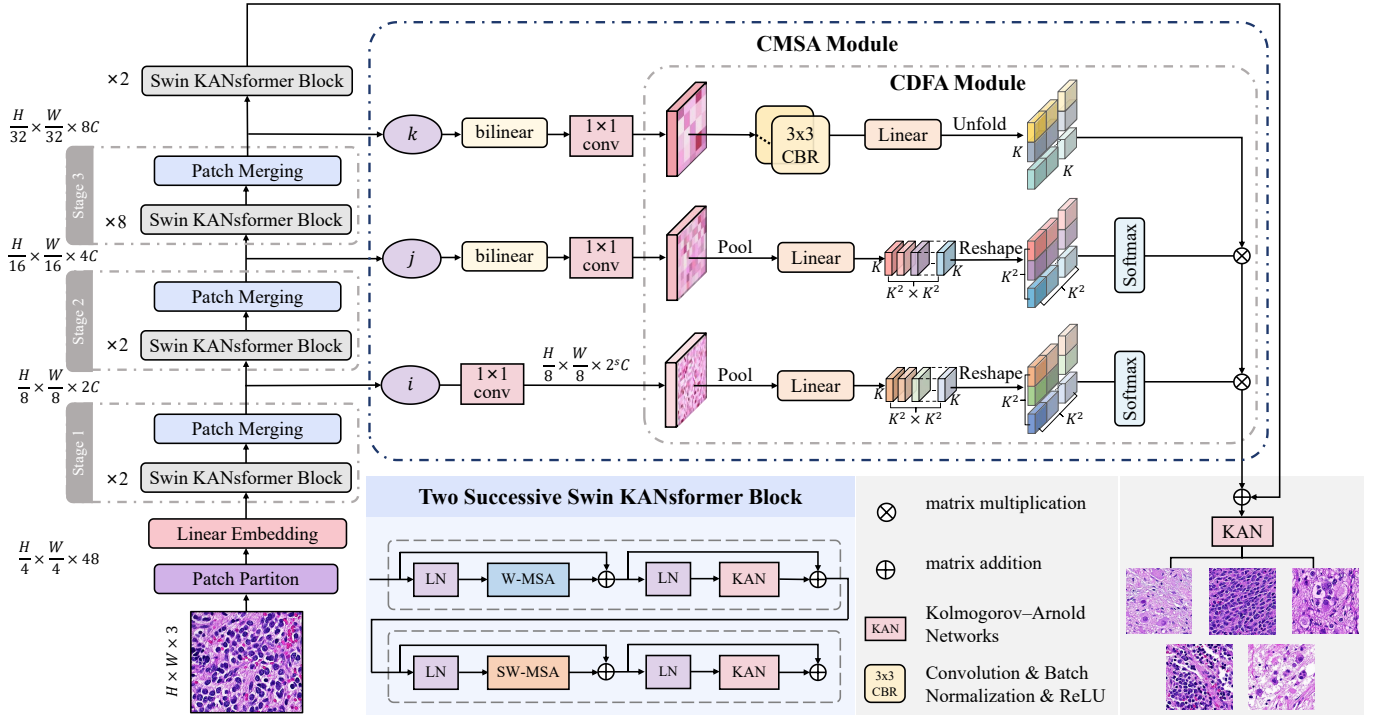


Fig. 1: Overall architecture of the CMSwinKAN model. The model consists mainly of the Swin KANsformer block and the contrast-driven Multi-Scale Feature Fusion Module. Within the Swin KANsformer block, W-MSA and SW-MSA are multi-head self-attention modules with regular and shifted window configurations, respectively.

D. Multiscale Methods in Medical Image Processing

Multiscale feature extraction and fusion are essential for enhancing image processing models. Chen et al. [26] proposed the CrossViT model, which uses a dual-branch Transformer with a cross-attention mechanism to fuse image patches of different sizes, improving image classification. Li et al. [27] introduced MViTv2, enhancing visual Transformers through relative position encoding and residual pooling connections. Ren et al. [28] presented Shunted Self-Attention, which aggregates multiscale features with heterogeneous receptive fields, overcoming the limitations of traditional self-attention. Jiao et al. [29] developed DilateFormer, utilizing multiscale dilated attention for efficient performance across various vision tasks.

In the medical image domain, Huo et al. [30] introduced the Hierarchical Multiscale Feature Fusion Network (HiFuse), which combines global and local features using adaptive fusion modules to improve robustness in complex classification tasks. Chen et al. [31] developed a leukocyte detection model based on deformable-DETR with multi-level feature fusion, enhancing detection accuracy through detailed cellular characteristics. Lei et al. [32] presented the ConDSeg framework, employing a contrast-driven feature enhancement strategy for better boundary recognition in image segmentation, achieving state-of-the-art performance.

III. METHOD

A. Overall Architecture

Fig. 1 illustrates the overall architecture of the CM-SwinKAN model (micro version), which is designed to ad-

dress the challenges of multi-scale feature representation and spatial dependency modeling in pathological image classification. This model is specifically tailored for the patch-level classification of pathological images from H&E-stained slides by combining a lightweight architecture with a strong interpretability.

The introduction of KAN layers significantly reduces model parameters by utilizing smaller embedding dimensions while enhancing feature representation and generalization [33]. The Swin KANsformer Block alternates between Window Multi-Head Self-Attention (W-MSA) and Shifted Window Multi-Head Self-Attention (SW-MSA) layers, replacing all multi-layer perception (MLP) layers with KAN layers, thereby boosting efficiency and interpretability.

The core structure of Contrastive-Driven Feature Augmentation (CDFA) in the CMSA module enhances multi-scale feature fusion by comparing attention across different scales, resulting in richer and more diagnostically meaningful insights [32]. These two modules work synergistically, enabling the CMSwinKAN model to efficiently and accurately classify H&E-stained pathological image patches and laying the foundation for WSI classification tasks.

B. Swin KANsformer Block

The Swin Transformer Block excels in image processing and medical image analysis compared to traditional vision Transformers due to its hierarchical feature maps and local window-based self-attention, which lower computational complexity and facilitate multi-scale feature extraction for high-resolution images. Its shifted window mechanism improves

information exchange, but it has limitations like constrained global receptive fields and high computational demands. We address these issues with the Swin KANsformer Block, an optimized version of the original.

The Swin KANsformer Block replaces traditional MLP layers in the Swin Transformer Block with KAN layers[33], improving the model’s ability to process complex H&E-stained pathological images. The model divides input RGB H&E-stained images into non-overlapping 4x4 patches (48 features each) via the Patch Partition module before projecting them into a feature dimension C using a linear embedding layer.

To facilitate the preservation of multi-scale features, we redefine the model’s stages. Aside from the final stage, which only contains d_3 Swin KANsformer Blocks, each stage includes d_i Swin KANsformer Blocks and a patch merging layer. In our base model, the number of Swin KANsformer Blocks across different stages is defined as $[d_0, d_1, d_2, d_3] = [2, 2, 8, 2]$. Due to the Patch Merging layers, the spatial dimensions of image features are progressively reduced after the first three stages, with sizes $[(\frac{H}{8}, \frac{W}{8}), (\frac{H}{16}, \frac{W}{16}), (\frac{H}{32}, \frac{W}{32})]$.

C. Contrastive-Driven Multi-Scale Aggregation Module

We analyze images at multiple scales to maintain spatial consistency. Our CMSA module effectively utilizes multi-scale features, incorporating the CDFA module to tackle challenges in medical image analysis.

Features from the first three stages of the Swin KANsformer are stored in a feature matrix and multiplied by a set of learnable weights $[i, j, k]$ to dynamically adjust the contribution of each stage. The features from the 2nd and 3rd stages, with sizes $[(\frac{H}{16}, \frac{W}{16}), (\frac{H}{32}, \frac{W}{32})]$, are upsampled via bilinear interpolation to the size of the first stage $(\frac{H}{8}, \frac{W}{8})$. The feature channels $[2C, 4C, 8C]$ are unified to $2^s C$ using 1×1 convolution blocks (in the base model, s is set to 1, so the features from the 1st stage do not require convolutional processing). After these operations, the features are fed into the CDFA module.

In the CDFA module, at each spatial location (i, j) , attention weights within a $K \times K$ window centered at (i, j) are computed by combining details from shallow and deep features. Specifically, the processed shallow features (features retained from the 1st and 2nd stages) F_1 and F_2 are passed through two different linear layers to compute attention weights A_1 and A_2 , respectively, where $A_1, A_2 \in \mathbb{R}^{\frac{H}{8} \times \frac{W}{8} \times K^2}$. The attention weight computation can be expressed as:

$$A_1 = W_1 \cdot F_1, A_2 = W_2 \cdot F_2, \quad (1)$$

where $W_1, W_2 \in \mathbb{R}^{2C \times K^4}$ are the linear transformation weight layers for the multi-scale feature maps from the 1st and 2nd stages, respectively. Each spatial location (i, j) in the two attention maps is then reshaped into $\hat{A}_{1,i,j} \in \mathbb{R}^{K \times K \times K^2}$ and $\hat{A}_{2,i,j} \in \mathbb{R}^{K \times K \times K^2}$, both activated by softmax.

The processed deep feature (retained from the 3rd stage) $F_3 \in \mathbb{R}^{\frac{H}{8} \times \frac{W}{8} \times 2C}$ is initially fused through two CBR blocks. A CBR block combines a convolution layer, batch normalization, and a ReLU activation function, simplifying the network construction process and improving training efficiency and

performance. The fused $2C$ -dimensional feature vector is then projected through a linear layer to a value vector $V_3 \in \mathbb{R}^{\frac{H}{8} \times \frac{W}{8} \times 2C}$. This value vector V_3 is then unfolded over local windows, aggregating neighborhood information for each position. Let $V_{\Delta_{i,j}} \in \mathbb{R}^{2C \times K^2}$ represent all values within a local window centered at (i, j) , defined as:

$$V_{\Delta_{i,j}} = \{V_{i+p-\lfloor \frac{K}{2} \rfloor, j+q-\lfloor \frac{K}{2} \rfloor}\}, \quad 0 \leq p, q < K. \quad (2)$$

The aggregation is performed in two steps:

$$\hat{V}_{\Delta_{i,j}} = \text{Softmax}(\hat{A}_{1,i,j}) \otimes (\text{Softmax}(\hat{A}_{2,i,j}) \otimes (V_{\Delta_{i,j}})), \quad (3)$$

where \otimes denotes matrix multiplication. Finally, the weighted feature values are densely aggregated to produce the final output feature map. Specifically, the aggregated feature at position (i, j) is:

$$\tilde{F}_{i,j} = \sum_{0 \leq m, n < K} \tilde{V}_{\Delta_{i+m-\lfloor \frac{K}{2} \rfloor, j+n-\lfloor \frac{K}{2} \rfloor}}^{i,j}. \quad (4)$$

D. KAN Classification Head

The multi-scale features from the CMSA module are combined with output residuals from the Swin KANsformer’s 4th stage, maintaining detail and semantic information for better image classification. The KAN serves as the classification head to improve non-linear fitting and performance, with each activation function as a learnable spline:

$$\phi(x) = w_b b(x) + w_s \text{spline}(x), \quad (5)$$

where $b(x)$ is a fixed basis function (e.g., SiLU), and $\text{spline}(x)$ is a learnable spline function.

KAN uses B-spline basis functions to create piecewise polynomials with local support, enabling efficient handling of high-dimensional data. The B-spline basis function serves as the core component of KAN for constructing piecewise polynomials. For input data x and a given set of grid points $t = \{t_0, t_1, \dots, t_n\}$, the B-spline basis function $N_{i,k}(x)$ is computed as follows:

$$N_{i,k}(x) = w_{i,k}(x) \cdot N_{i,k-1}(x) + (1 - w_{i+1,k}(x)) \cdot N_{i+1,k-1}(x), \quad (6)$$

where

$$w_{i,k}(x) = \frac{x - t_i}{t_{i+k} - t_i}. \quad (7)$$

The recursive formulation $N_{i,k}(x)$ ensures efficient computation of B-spline basis functions, while their local support lets the KAN head model complex feature spaces efficiently.

For WSI-level pathological diagnosis, a heuristic soft voting classification process is developed that combines individual patch classifications with global feature information for a final label, using weighted slice importance for more robust results than hard voting, illustrated in Fig. 2. We also train an SVM model to identify specific tissue structures like neuropil and Schwannian stroma. Further details on the voting mechanism and SVM training will follow.

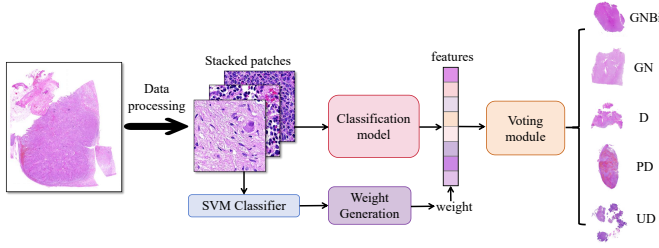


Fig. 2: The architecture of the proposed WSI voting mechanism. After feature classification of the slices using an SVM classifier, weights are dynamically assigned based on classification confidence, ultimately implementing a weighted soft voting strategy for decision.

E. WSI Voting Classification Mechanism

1) *Voting Mechanism Design*: WSI classification via hard voting assigns equal weight to each patch and determines the final result by majority rule, but its precision is relatively low. To enhance accuracy, we designed a soft voting approach that incorporates prior knowledge. In pathological analysis, patches with neuropil indicate potential malignancy (ganglioneuroblastoma, intermixed (GNBi) or NB), while patches with Schwannian stroma may indicate ganglioneuroma (GN). If Schwannian stroma comprises 50% or more of the patch, it suggests GNBi or GN; otherwise, it leans towards NB.

We can derive the voting weights for all patches in the WSI. Integrating these weights with classification results yields the final WSI classification $\text{Label}_{\text{WSI}}$:

$$P \in R^{N \times C}, W \in R^{N \times C},$$

$$\mathbf{s} = (W \circ P)^\top \begin{bmatrix} 1 \\ 1 \\ \vdots \\ 1 \end{bmatrix} = \begin{bmatrix} \sum_{i=1}^N w_{i,1} p_{i,1} \\ \sum_{i=1}^N w_{i,2} p_{i,2} \\ \vdots \\ \sum_{i=1}^N w_{i,C} p_{i,C} \end{bmatrix}, \quad (8)$$

$$\alpha = [1 \quad 1 \quad \cdots \quad 1] \left(W \begin{bmatrix} 1 \\ 1 \\ \vdots \\ 1 \end{bmatrix} \right) = \sum_{i=1}^N \sum_{c=1}^C w_{i,c}, \quad (9)$$

$$\hat{p} = \frac{\mathbf{s}}{\alpha}, \text{Label}_{\text{WSI}} = \arg \max \hat{p}_c, \quad c \in \{1, \dots, C\}, \quad (10)$$

where $P_{i,C}$ represents the classification category and probability of the C -th patch, and $w_{i,C}$ denotes the corresponding voting weight.

2) *Training and Application of the SVM Model*: Leveraging the features extracted by the patch classification model CM-SwinKAN, we train a multi-class SVM model to determine whether a patch contains neuropil, Schwannian stroma, or other tissue components. Based on the SVM prediction results, the voting weight of the patch w_{patch} is determined as follows:

$$w_{\text{patch}} = \alpha \cdot P_1 + \beta \cdot P_2, \quad (11)$$

where P_1 and P_2 are the neuropil and Schwannian stroma probabilities, respectively. α and β are weighting coefficients used to control the importance of different tissue components, with $\alpha > \beta$ emphasizing the significance of neuropil. If the SVM classifies the patch as other tissue, then $w_{\text{patch}} = \gamma$, where γ is a lower baseline weight.

IV. EXPERIMENTS

A. Data Collection and Processing

There is a shortage of pathological datasets for NB due to the complexities of data collection and annotation. To address this issue, we established a private Pediatric Peripheral Neuroblastic Tumor dataset (PpNTs), derived from 102 pediatric patients at the Children's Hospital, Zhejiang University School of Medicine. This dataset includes three major pathological categories: NB with its histological subtypes — undifferentiated (UD), poorly differentiated (PD), and differentiated (D); GNBi; and GN. In total, 304 WSIs were acquired from these cases. Digitization was performed using a Panoramic SCAN II digital scanner (3DHISTECH Ltd, Budapest, Hungary) at a magnification of 20 \times . The dataset details are shown in Fig. 4, and the summary statistics are provided in Table I. The study and the dataset was ethically approved by the Academic Ethics Committee of Children's Hospital Zhejiang University School of Medicine (IRB No. 2023-IRB-0287-P-01). We applied for an informed consent waiver.

1) *Sliding Window Segmentation*: As shown in Fig. 3, a sliding window algorithm with a non-overlapping strategy is used, starting from the top-left corner of the WSI (0,0). The window slides horizontally with a step size of 512 pixels, discarding right and bottom areas that can't be fully covered by a 512 \times 512 pixel window to avoid invalid data.

2) *Data Quality Improvement*: This study adopts a two-stage filtering rule: patches with over 50% white pixels ($\text{RGB} \geq 245$) are discarded, as they likely indicate a blank background or staining defect. Patches with over 50% red pixels are classified as dense red blood cell areas and are also discarded, as they may obscure important pathological features.

B. Comparison on Existing Datasets

To validate the model's generalization ability, we used the public BreakHis dataset, which contains 7,909 histopathological images from 82 patients collected by the P&D laboratory in Brazil, categorized into eight types at various magnifications. We focused on images with $\times 400$ magnification. To tackle class imbalance, data augmentation was applied to the training set, increasing the number of patches from 1,427 to 6,109, while the testing set remained at 393 patches.

C. Experimental Setup

The experiments utilized an NVIDIA Tesla V100-SXM2 GPU with 32GB of graphic memory, running on Python 3.8.20 and PyTorch 2.4.1 with CUDA 12.1. Training on our private dataset lasted for 30 epochs with a batch size of 64, totaling approximately 75 hours.

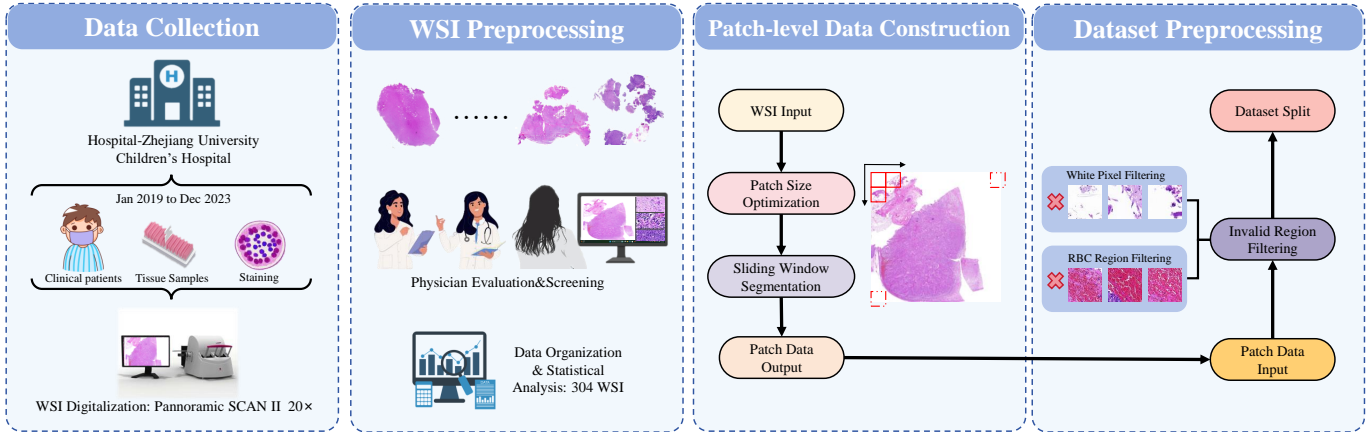


Fig. 3: Medical data processing workflow based on pathological sections, which includes four main stages: (1) Data Collection, covering the collection of clinical patient tissue samples, tissue sample processing, and staining, as well as WSI scanning; (2) WSI preprocessing, involving physician evaluation and screening of WSIs and data organization; (3) Patch-level Data Construction, including determining patch size and sliding window segmentation of slices; (4) Dataset Preprocessing, covering invalid region filtering and dataset splitting, ultimately providing structured data support for model training and evaluation.

TABLE I: Number of WSIs and patches per category in our private PpNTs dataset.

Class	GN		GNBi		PD		D		UD	
	WSI	Patch	WSI	Patch	WSI	Patch	WSI	Patch	WSI	Patch
Train	48	536,013	50	484,792	44	432,627	49	474,440	50	451,986
Test	12	110,519	13	138,995	12	116,903	13	151,007	13	103,438

TABLE II: Settings and parameters of different versions of CMSwinKAN models.

Model	embed_dim	num_heads	Params	FLOPs
CMSwinKAN-mini	24	(2, 4, 8, 16)	1.29M	0.21G
CMSwinKAN-micro	24	(4, 8, 16, 32)	1.32M	0.22G
CMSwinKAN-tiny	56	(4, 8, 16, 32)	5.52M	1.08G

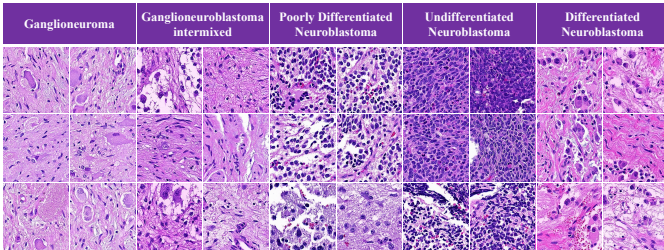


Fig. 4: Visual representation of our private PpNTs dataset.

Input images were resized to 224×224 pixels, and the model was initialized randomly using a He normal distribution[34], and the AdamW optimizer was paired with a cosine annealing strategy. We set $\alpha = 1$ for neuropil and $\beta = 8$ for Schwannian stroma, with $\gamma = 1$ assigned to non-key tissue regions.

D. Comparative Experiments

1) *Model Performance Comparison:* Table III shows that we conducted comparative experiments on the PpNTs dataset, evaluating our model against other typical classification models, general large models in pathology, and advanced pathological image classification models. Compared to other typical

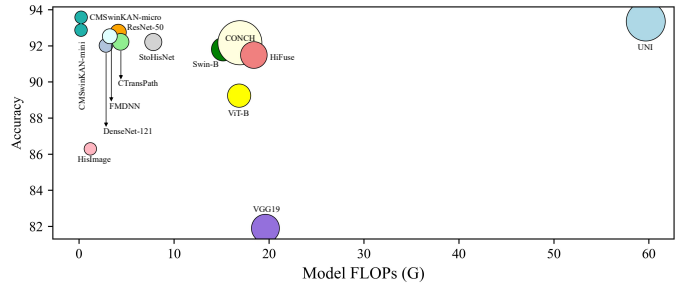


Fig. 5: Relationship between ACC, parameters, and FLOPs of CMSwinKAN and other advanced models on our private PpNTs dataset. The size of each circle represents the number of parameters for each model.

models, general large models in pathology, or advanced pathological image classification models, CMSwinKAN demonstrates significant advantages in handling microscopic image classification tasks. Fig. 7 and Fig. 8 demonstrate the confusion matrices and AUC curves of CMSwinKAN tested on the PpNTs and BreakHis datasets.

Compared to the baseline models Swin Transformer and Vision Transformer, the ACC is improved by 1.77% and

TABLE III: Comparison of CMSwinKAN with other advanced models on our private PpNTs and public BreakHis datasets.

Dataset	PpNTs					BreakHis				
Model	ACC	BACC	KAPPA	F1	AUROC	ACC	BACC	KAPPA	F1	AUROC
General methods										
VGGNet [35]	81.89	81.52	74.37	81.76	97.02	48.09	23.57	21.44	41.37	67.71
ResNet-50 [36]	92.75	92.35	90.94	92.73	<u>99.43</u>	68.45	55.61	47.65	67.40	92.37
DenseNet [37]	92.02	91.73	89.71	91.93	99.36	83.21	80.81	77.33	83.64	98.25
Vision Transformer [38]	89.24	89.12	85.90	89.23	98.79	68.45	59.84	61.27	67.58	91.03
Swin Transformer [39]	91.81	91.68	89.64	91.81	99.30	75.82	71.22	68.38	76.06	96.37
Pathological large-scale pre-trained general models										
UNI [19]	<u>93.35</u>	<u>93.12</u>	<u>91.64</u>	<u>93.29</u>	99.43	78.88	69.91	72.07	71.41	97.03
CTransPath [18]	92.22	92.11	90.22	92.24	99.36	83.46	86.62	78.92	83.79	<u>98.52</u>
CONCH [20]	92.17	92.01	90.32	92.15	95.66	<u>86.77</u>	<u>86.99</u>	86.98	<u>86.81</u>	94.73
Pathological classification model										
HisImage [40]	86.29	86.26	82.78	86.21	98.00	64.63	55.96	52.50	57.59	84.43
FMDNN [23]	92.53	92.30	89.81	92.48	99.41	86.32	81.68	84.71	86.14	96.57
StoHisNet [41]	92.21	92.03	90.87	92.18	99.33	74.84	68.33	67.32	74.24	94.26
HiFuse [30]	91.49	91.40	89.31	91.49	99.29	62.84	47.93	48.78	60.59	87.02
Ours										
CMSwinKAN-micro	93.58	93.42	92.12	93.57	99.53	87.79	87.56	<u>85.69</u>	88.04	98.80

TABLE IV: Comparison of CMSwinKAN with other advanced models for WSI classification on our private PpNTs dataset.

Model	ACC	BACC	KAPPA	F1
General methods				
VGGNet [35] (hard vote)	92.06	91.79	90.07	91.88
VGGNet [35] (soft vote)	93.65	93.46	92.06	93.55
ResNet-50 [36] (hard vote)	98.41	98.33	98.01	98.39
ResNet-50 [36] (soft vote)	98.41	98.33	98.01	98.39
DenseNet [37] (hard vote)	98.41	98.33	98.01	98.39
DenseNet [37] (soft vote)	98.41	98.33	98.01	98.39
Vision Transformer [38] (hard vote)	98.41	98.33	98.01	98.39
Vision Transformer [38] (soft vote)	98.41	98.33	98.01	98.39
Swin Transformer [39] (hard vote)	98.41	98.33	98.01	98.39
Swin Transformer [39] (soft vote)	98.41	98.33	98.01	98.39
Pathological large-scale pre-trained general models				
UNI [19] (hard vote)	98.41	98.33	98.01	98.39
UNI [19] (soft vote)	98.41	98.33	98.01	98.39
CTransPath [18] (hard vote)	98.41	98.33	98.01	98.39
CTransPath [18] (soft vote)	98.41	98.33	98.01	98.39
CONCH [20] (hard vote)	98.41	98.33	98.01	98.39
CONCH [20] (soft vote)	98.41	98.33	98.01	98.39
Pathological classification models				
HisImage [40] (hard vote)	95.24	95.13	94.04	95.20
HisImage [40] (soft vote)	96.83	96.79	96.03	96.82
FMDNN [23] (hard vote)	98.41	98.33	98.01	98.39
FMDNN [23] (soft vote)	98.41	98.33	98.01	98.39
StoHisNet [41] (hard vote)	98.41	98.33	98.01	98.39
StoHisNet [41] (soft vote)	98.41	98.33	98.01	98.39
HiFuse [30] (hard vote)	98.41	98.33	98.01	98.39
HiFuse [30] (soft vote)	98.41	98.33	98.01	98.39
Ours				
CMSwinKAN-micro (hard vote)	98.41	98.33	98.01	98.39
CMSwinKAN-micro (soft vote)	100.00	100.00	100.00	100.00

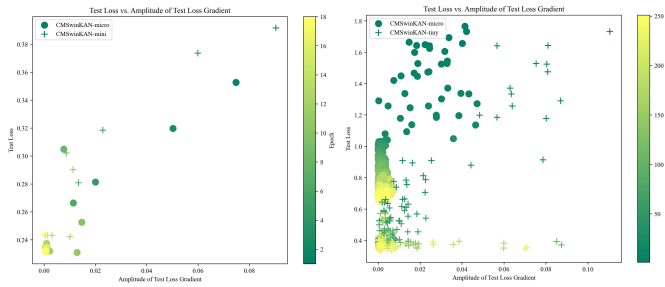


Fig. 6: The loss-gradient plots for different versions of the CMSwinKAN models evaluated on our private PpNTs and public BreakHis datasets.

4.34%, respectively. This improvement can be attributed to integrating the CMSA module and KAN in CMSwinKAN, which effectively captures fine-grained features and high-level semantic information in pathological images.

Our model, using random initialization without pre-training, outperformed CONCH and UNI, which were pre-trained on large pathological datasets. As shown in Fig. 5, CMSwinKAN combines high accuracy with a lightweight design, giving it a distinct advantage over other models.

We compared our CMSwinKAN with advanced pathological image classification models like HisImage [40], FMDNN [23], and HiFuse [30], which struggle with similar categorical features. Under the same training conditions, CMSwinKAN outperformed them in all metrics, with KAPPA scores of 92.12% compared to their 82.78%, 89.81%, and 89.31%. When compared to the improved baseline model CTransPath[18] and StoHisNet[41], CMSwinKAN also improved ACC by 1.37%, highlighting its architectural advantages. For WSI classification, the CMSwinKAN model demonstrates significant clinical value. With a soft voting strategy, it achieved 98.41% ACC and 98.33% BACC. This strategy notably improved VGGNet’s performance, raising ACC from 92.06% to 93.65% and BACC from 91.79% to 93.46%.

2) *Validation of Model Generalization Ability:* To further validate the generalization capability of the proposed CMSwinKAN model, we compared it with other typical classification models, large models in pathology, and advanced pathological image classification models on the publicly available breast cancer dataset, BreakHis. Table III with BreakHis dataset shows that CMSwinKAN demonstrated strong generalization ability on the imbalanced dataset, achieving excellent results across all metrics. Fig. 6 depicts the loss and gradients on the test set during training.

We conducted WSI classification experiments on the BreakHis dataset to further confirm its generalization ability. As shown in Table V, when using a hard voting strategy, CMSwinKAN exhibited outstanding performance even in imbalanced data scenarios. This result aligns with findings from the PpNTs dataset, confirming that the model adapts well to pathological image classification across various data distributions through multi-scale feature interaction in the CMSA module and nonlinear mapping in the KAN layer.

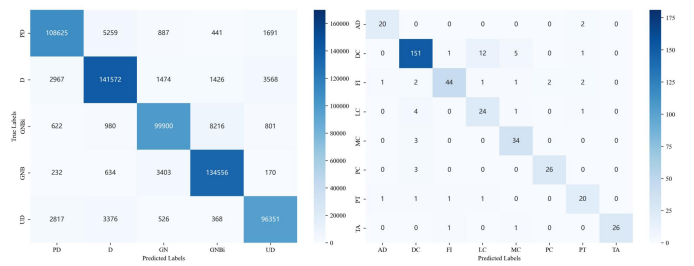


Fig. 7: Confusion matrices of CMSwinKAN on our private PpNTs and public BreakHis tested datasets.

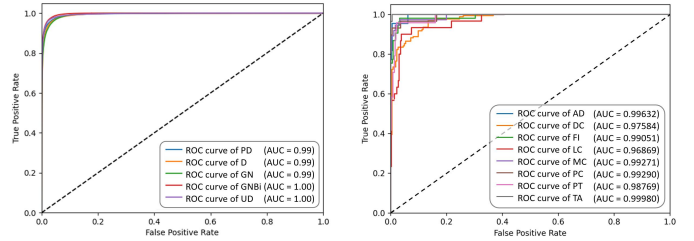


Fig. 8: ROC curves of CMSwinKAN on our private PpNTs and public BreakHis tested datasets.

E. Ablation Experiments

Our ablation experiments further analyzed the impact of the KAN network, CDFA component, and CMSA on classification performance across both datasets. Table VI confirmed that these three modules positively influence the model’s classification performance. Specifically:

Impact of the KAN Network: In the SwinKANsformer Block, the KAN network replaces the traditional MLP layer, improving nonlinear feature extraction and interpretability. Switching to the MLP layer leads to a drop in classification performance: ACC decreases from 93.58% to 92.29%, BACC from 93.42% to 92.09%, and KAPPA and F1 scores decline from 92.12% and 93.57% to 90.93% and 92.28%. This drop occurs due to a reduced ability to capture fine details in pathological images, leading to cell type confusion.

Replacing the CDFA Module with a Linear Layer: The CDFA module improves the model’s learning by effectively comparing features across various scales. Replacing it with a linear layer leads to significant feature loss, with KAPPA decreasing by 1.29% and F1 scores dropping by 0.7%. This underlines the CDFA module’s essential role in multi-scale feature fusion, enhancing the model’s integration of high-level semantic and detailed edge information in pathological images.

Removing the CMSA Module: The CMSA module enhances the CDFA module by optimizing multi-scale feature contributions and capturing both long-range dependencies and local features in pathological slice images while reducing contamination from low-density scales. Removing the CMSA module significantly decreases performance metrics: BACC by 1.28%, and KAPPA by 1.38%. This decline is greater than that seen when the CDFA module is replaced with a linear layer, underscoring the CMSA module’s crucial role in high-density feature extraction and multi-scale learning.

TABLE V: Comparison of CMSwinKAN with other advanced models using hard voting for WSI classification (BreakHis).

Model	ACC	BACC	KAPPA	F1
General methods				
VGGNet [35] (hard vote)	46.91	33.45	32.00	23.60
ResNet-50 [36] (hard vote)	60.49	63.36	51.98	54.98
DenseNet [37] (hard vote)	93.83	94.21	91.75	92.67
Vision Transformer [38] (hard vote)	66.67	60.28	55.50	57.88
Swin Transformer [39] (hard vote)	80.25	75.54	73.80	73.71
Pathological large-scale pre-trained general models				
UNI [19] (hard vote)	88.89	78.99	84.70	82.49
CTransPath [18] (hard vote)	92.59	<u>94.56</u>	90.17	91.84
CONCH [20] (hard vote)	<u>95.05</u>	93.75	<u>93.28</u>	<u>94.51</u>
Pathological classification models				
HisImage [40] (hard vote)	75.31	69.36	65.60	69.26
FMDNN [23] (hard vote)	92.59	93.73	90.17	91.37
StoHisNet [41] (hard vote)	85.23	75.84	67.09	84.23
HiFuse [30] (hard vote)	64.20	43.76	47.43	43.80
Ours				
CMSwinKAN-tiny (hard vote)	95.06	96.69	93.40	95.34

TABLE VI: Ablation studies of CMSwinKAN on our private PpNTs and public BreakHis datasets.

Dataset	PpNTs					BreakHis				
	Model	ACC	BACC	KAPPA	F1	AUROC	ACC	BACC	KAPPA	F1
w/o KAN	92.29	92.09	<u>90.93</u>	92.28	99.39	80.66	79.59	77.31	80.90	97.81
w/o CDFA	<u>92.89</u>	<u>92.73</u>	90.93	<u>92.88</u>	99.44	<u>82.18</u>	<u>82.41</u>	75.75	<u>82.60</u>	<u>98.14</u>
w/o CMSA	92.50	92.24	90.85	92.49	99.42	79.64	81.40	<u>77.44</u>	80.06	97.78
CMSwinKAN	93.58	93.42	92.12	93.57	99.53	87.79	87.56	85.69	88.04	98.80

V. CONCLUSION

This paper proposed a model named CMSwinKAN for the pathological-grade diagnosis NB pathological slices stained with H&E. The model innovatively integrates multi-scale features and comparative learning strategies, effectively addressing the key issues such as insufficient feature integration of existing methods, poor model interpretability, and the easy contamination of multi-scale features by low-density information. Additionally, a heuristic soft voting mechanism was designed, guided by clinical insights, to achieve an efficient transition from patch-level classification to WSI-level classification. Experiments on private PpNTs and public BreakHis datasets demonstrate that this method significantly outperforms the prior art. Particularly, the interpretable output of the model is highly consistent with the pathological diagnostic criteria, providing reliable support for clinical AI-assisted diagnosis. Future work will focus on multi-center data verification and exploring the fusion application with molecular diagnosis to further enhance the clinical practical value.

REFERENCES

- [1] R. Bagatell, J. R. Park, S. Acharya, J. Aldrink, J. Allison, E. Alva, C. Arndt, D. Benedetti, E. Brown, S. Cho *et al.*, “Neuroblastoma, version 2.2024, nccn clinical practice guidelines in oncology,” *Journal of the National Comprehensive Cancer Network*, vol. 22, no. 6, pp. 413–433, 2024.
- [2] I. S. Fetahu, W. Esser-Skala, R. Dnyansagar, S. Sindelar, F. Rifatbegovic, A. Bileck, L. Skos, E. Bozsaky, D. Lazic, L. Shaw *et al.*, “Single-cell transcriptomics and epigenomics unravel the role of monocytes in neuroblastoma bone marrow metastasis,” *Nature communications*, vol. 14, no. 1, p. 3620, 2023.
- [3] Y. Liu, Y. Jia, C. Hou, N. Li, N. Zhang, X. Yan, L. Yang, Y. Guo, H. Chen, J. Li *et al.*, “Pathological prognosis classification of patients with neuroblastoma using computational pathology analysis,” *Computers in Biology and Medicine*, vol. 149, p. 105980, 2022.
- [4] Y. Xie, Z. Liu, J. Chen, W. Zhang, J. Zhao, and J. Ma, “Sd-mil: Multiple instance learning with dual perception of scale and distance information fusion for whole slide image classification,” *Expert Systems with Applications*, p. 126831, 2025.
- [5] P. Liu, L. Ji, X. Zhang, and F. Ye, “Pseudo-bag mixup augmentation for multiple instance learning-based whole slide image classification,” *IEEE Transactions on Medical Imaging*, vol. 43, no. 5, pp. 1841–1852, 2024.
- [6] H. Xu, Q. Xu, F. Cong, J. Kang, C. Han, Z. Liu, A. Madabhushi, and C. Lu, “Vision transformers for computational histopathology,” *IEEE Reviews in Biomedical Engineering*, vol. 17, pp. 63–79, 2023.
- [7] C.-W. Wang, H. Muzakky, N. P. Firdi, T.-C. Liu, P.-J. Lai, Y.-C. Wang, M.-H. Yu, and T.-K. Chao, “Deep learning to assess microsatellite instability directly from histopathological whole slide images in endometrial cancer,” *NPJ Digital Medicine*, vol. 7, no. 1, p. 143, 2024.
- [8] S. Yan, B. Yang, A. Chen, X. Zhao, and S. Zhang, “Multi-scale convolutional attention frequency-enhanced transformer network for medical image segmentation,” *Information Fusion*, p. 103019, 2025.
- [9] Y. Chen, B. Zou, Z. Guo, Y. Huang, Y. Huang, F. Qin, Q. Li, and C. Wang, “Scunet++: Swin-unet and cnn bottleneck hybrid architecture with multi-fusion dense skip connection for pulmonary embolism ct image segmentation*,” in *2024 IEEE/CVF Winter Conference on Applications of Computer Vision (WACV)*, 2024, pp. 7759–7767.
- [10] Y. Chen, Z. Zhu, S. Zhu, L. Qiu, B. Zou, F. Jia, Y. Zhu, C. Zhang, Z. Fang, F. Qin *et al.*, “Sckansformer: Fine-grained classification of bone marrow cells via kansformer

- backbone and hierarchical attention mechanisms,” *IEEE Journal of Biomedical and Health Informatics*, 2024.
- [11] N. A. Wani, R. Kumar, J. Bedi, I. Rida *et al.*, “Explainable ai-driven iomt fusion: Unravelling techniques, opportunities, and challenges with explainable ai in healthcare,” *Information Fusion*, p. 102472, 2024.
 - [12] J.-G. Yu, Z. Wu, Y. Ming, S. Deng, Q. Wu, Z. Xiong, T. Yu, G.-S. Xia, Q. Jiang, and Y. Li, “Bayesian collaborative learning for whole-slide image classification,” *IEEE Transactions on Medical Imaging*, vol. 42, no. 6, pp. 1809–1821, 2023.
 - [13] J. Yu, X. Wang, T. Ma, X. Li, and Y. Xu, “Patch-slide discriminative joint learning for weakly-supervised whole slide image representation and classification,” in *International Conference on Medical Image Computing and Computer-Assisted Intervention*. Springer, 2024, pp. 713–722.
 - [14] S. Gheisari, D. R. Catchpoole, A. Charlton, Z. Melegh, E. Gradhand, and P. J. Kennedy, “Computer aided classification of neuroblastoma histological images using scale invariant feature transform with feature encoding,” *Diagnostics*, vol. 8, no. 3, p. 56, 2018.
 - [15] S. Gheisari, D. R. Catchpoole, A. Charlton, and P. J. Kennedy, “Convolutional deep belief network with feature encoding for classification of neuroblastoma histological images,” *Journal of Pathology Informatics*, vol. 9, no. 1, p. 17, 2018.
 - [16] L. Hou, D. Samaras, T. M. Kurc, Y. Gao, J. E. Davis, and J. H. Saltz, “Patch-based convolutional neural network for whole slide tissue image classification,” in *2016 IEEE Conference on Computer Vision and Pattern Recognition (CVPR)*, 2016, pp. 2424–2433.
 - [17] H. Li, C. Zhu, Y. Zhang, Y. Sun, Z. Shui, W. Kuang, S. Zheng, and L. Yang, “Task-specific fine-tuning via variational information bottleneck for weakly-supervised pathology whole slide image classification,” in *2023 IEEE/CVF Conference on Computer Vision and Pattern Recognition (CVPR)*, 2023, pp. 7454–7463.
 - [18] X. Wang, S. Yang, J. Zhang, M. Wang, J. Zhang, W. Yang, J. Huang, and X. Han, “Transformer-based unsupervised contrastive learning for histopathological image classification,” *Medical Image Analysis*, vol. 81, p. 102559, 2022.
 - [19] R. J. Chen, T. Ding, M. Y. Lu, D. F. Williamson, G. Jaume, A. H. Song, B. Chen, A. Zhang, D. Shao, M. Shaban *et al.*, “Towards a general-purpose foundation model for computational pathology,” *Nature Medicine*, vol. 30, no. 3, pp. 850–862, 2024.
 - [20] M. Y. Lu, B. Chen, D. F. Williamson, R. J. Chen, I. Liang, T. Ding, G. Jaume, I. Odintsov, L. P. Le, G. Gerber *et al.*, “A visual-language foundation model for computational pathology,” *Nature Medicine*, vol. 30, no. 3, pp. 863–874, 2024.
 - [21] S. Azizi, L. Culp, J. Freyberg, B. Mustafa, S. Baur, S. Kornblith, T. Chen, N. Tomasev, J. Mitrović, P. Strachan *et al.*, “Robust and data-efficient generalization of self-supervised machine learning for diagnostic imaging,” *Nature Biomedical Engineering*, vol. 7, no. 6, pp. 756–779, 2023.
 - [22] K. Zormpas-Petridis, R. Noguera, D. K. Ivankovic, I. Roxanis, Y. Jamin, and Y. Yuan, “Superhistopath: A deep learning pipeline for mapping tumor heterogeneity on low-resolution whole-slide digital histopathology images,” *Frontiers in oncology*, vol. 10, p. 586292, 2021.
 - [23] W. Ding, T. Zhou, J. Huang, S. Jiang, T. Hou, and C.-T. Lin, “Fmdnn: A fuzzy-guided multigranular deep neural network for histopathological image classification,” *IEEE Transactions on Fuzzy Systems*, 2024.
 - [24] T. Stegmüller, B. Bozorgtabar, A. Spahr, and J.-P. Thiran, “Scorenet: Learning non-uniform attention and augmentation for transformer-based histopathological image classification,” in *2023 IEEE/CVF Winter Conference on Applications of Computer Vision (WACV)*, 2023, pp. 6170–6179.
 - [25] Y. Liu, M. Yin, and S. Sun, “Detexnet: Accurately diagnosing frequent and challenging pediatric malignant tumors,” *IEEE Transactions on Medical Imaging*, vol. 40, no. 1, pp. 395–404, 2020.
 - [26] C.-F. R. Chen, Q. Fan, and R. Panda, “Crossvit: Cross-attention multi-scale vision transformer for image classification,” in *2021 IEEE/CVF International Conference on Computer Vision (ICCV)*, 2021, pp. 357–366.
 - [27] Y. Li, C.-Y. Wu, H. Fan, K. Mangalam, B. Xiong, J. Malik, and C. Feichtenhofer, “Mvitv2: Improved multiscale vision transformers for classification and detection,” in *2022 IEEE/CVF Conference on Computer Vision and Pattern Recognition (CVPR)*, 2022, pp. 4804–4814.
 - [28] S. Ren, D. Zhou, S. He, J. Feng, and X. Wang, “Shunted self-attention via multi-scale token aggregation,” in *2022 IEEE/CVF Conference on Computer Vision and Pattern Recognition (CVPR)*, 2022, pp. 10 853–10 862.
 - [29] J. Jiao, Y.-M. Tang, K.-Y. Lin, Y. Gao, A. J. Ma, Y. Wang, and W.-S. Zheng, “Dilateformer: Multi-scale dilated transformer for visual recognition,” *IEEE Transactions on Multimedia*, vol. 25, pp. 8906–8919, 2023.
 - [30] X. Huo, G. Sun, S. Tian, Y. Wang, L. Yu, J. Long, W. Zhang, and A. Li, “Hifuse: Hierarchical multi-scale feature fusion network for medical image classification,” *Biomedical Signal Processing and Control*, vol. 87, p. 105534, 2024.
 - [31] Y. Chen, C. Zhang, B. Chen, Y. Huang, Y. Sun, C. Wang, X. Fu, Y. Dai, F. Qin, Y. Peng *et al.*, “Accurate leukocyte detection based on deformable-detr and multi-level feature fusion for aiding diagnosis of blood diseases,” *Computers in Biology and Medicine*, vol. 170, p. 107917, 2024.
 - [32] M. Lei, H. Wu, X. Lv, and X. Wang, “Condseg: A general medical image segmentation framework via contrast-driven feature enhancement,” *arXiv preprint arXiv:2412.08345*, 2024.
 - [33] Z. Liu, Y. Wang, S. Vaidya, F. Ruehle, J. Halverson, M. Soljagic, T. Y. Hou, and M. Tegmark, “KAN: Kolmogorov–arnold networks,” in *The Thirteenth International Conference on Learning Representations*, 2025.
 - [34] K. He, X. Zhang, S. Ren, and J. Sun, “Delving deep into rectifiers: Surpassing human-level performance on imagenet classification,” *IEEE Computer Society*, 2015.
 - [35] K. Simonyan and A. Zisserman, “Very deep convolutional networks for large-scale image recognition,” *arXiv preprint arXiv:1409.1556*, 2014.
 - [36] K. He, X. Zhang, S. Ren, and J. Sun, “Deep residual learning for image recognition,” in *2016 IEEE Conference on Computer Vision and Pattern Recognition (CVPR)*, 2016, pp. 770–778.
 - [37] G. Huang, Z. Liu, L. Van Der Maaten, and K. Q. Weinberger, “Densely connected convolutional networks,” in *2017 IEEE Conference on Computer Vision and Pattern Recognition (CVPR)*, 2017, pp. 4700–4708.
 - [38] A. Dosovitskiy, L. Beyer, A. Kolesnikov, D. Weissenborn, X. Zhai, T. Unterthiner, M. Dehghani, M. Minderer, G. Heigold, S. Gelly, J. Uszkoreit, and N. Houlsby, “An image is worth 16x16 words: Transformers for image recognition at scale,” *ICLR*, 2021.
 - [39] Z. Liu, Y. Lin, Y. Cao, H. Hu, Y. Wei, Z. Zhang, S. Lin, and B. Guo, “Swin transformer: Hierarchical vision transformer using shifted windows,” in *2021 IEEE/CVF International Conference on Computer Vision (ICCV)*, 2021, pp. 10012–10022.
 - [40] M. Ding, A. Qu, H. Zhong, Z. Lai, S. Xiao, and P. He, “An enhanced vision transformer with wavelet position embedding for histopathological image classification,” *Pattern Recognition*, vol. 140, p. 109532, 2023.
 - [41] B. Fu, M. Zhang, J. He, Y. Cao, Y. Guo, and R. Wang, “Stohisnet: A hybrid multi-classification model with cnn and transformer for gastric pathology images,” *Computer Methods and Programs in Biomedicine*, vol. 221, p. 106924, 2022.